

# SPACEBORNE LASER FILAMENTATION: A NEW REMOTE SENSING TOOL FOR ATMOSPHERIC SPECTROSCOPY?

I. Dicaire<sup>a,1,2,\*</sup>, V. Jukna<sup>b,1</sup>, C. Praz<sup>a</sup>, C. Milian<sup>b</sup>, L. Summerer<sup>a</sup>, A. Couairon<sup>b,\*</sup>

<sup>a</sup>ESA Advanced Concepts Team, Keplerlaan 1, 2201 Noordwijk, The Netherlands

<sup>b</sup>Centre de Physique Théorique, École Polytechnique, F-91128, Palaiseau, France

---

## Abstract

This paper presents the first proof-of-concept of space-borne laser filamentation for atmospheric remote sensing. Our results indicate that a filament can form at an altitude of 7 km associated with the generation of a white-light continuum resulting from strong pulse splitting and beam collapse. The theoretical model includes a realistic representation of the stratified atmosphere and accounts for multi-species ionisation and the dependence of air density upon the molecule type and altitude profile. A preliminary assessment of the general payload parameters is also performed for a platform orbiting at a 400-km altitude. We find that operating conditions for the proposed space-borne white-light lidar concept are already available with current ground-based mobile laser technology and within reach of future space laser systems.

**Keywords:** Remote Sensing, Lidar Missions, Femtosecond Lasers, Nonlinear Optics, White-light Lidar

---

## 1. INTRODUCTION

Remote sensing of the atmosphere via Earth-orbiting satellites provide essential information in the field of climate science and atmospheric chemistry. Driven by the need to improve our understanding of climate change, remote sensing instrumentation aims at providing high resolution measurements of key trace constituents on a global scale with high accuracy [1]. Monitoring of long-lived greenhouse gases such as carbon dioxide and methane is required at adequate spatial and temporal sampling to disentangle anthropogenic from natural sources. Monitoring of short-lived pollutants such as volatile organic compounds and radiatively active gases such as tropospheric ozone and nitrogen oxides is also required because of their impact on human health and climate change [2–5]. Furthermore ozone molecules play a critical role in atmospheric chemistry; they are involved in chemical reactions producing the hydroxyl radical, which provides a natural self-cleansing mechanism to eliminate atmospheric pollutants [6]. Ozone chemistry is a complex phenomena which needs to be better understood in view of global warming, ozone loss, and tropospheric pollution [1, 5, 7, 8]. To help answer these questions multispectral synoptic observations of key atmospheric trace constituents at different atmospheric depths are required at sufficient spectral and spatial resolution with adequate accuracy [9, 10].

Over the past years, a variety of spaceborne instruments has been developed to improve our understanding of ozone chemistry and climate change [11–16]. Imaging spectrometers can provide column-integrated measurements of several critical atmospheric constituents along the line of sight in the nadir and sun glint modes [11]. To obtain vertical profiles in the stratosphere, the solar occultation mode can be used, however suffering from large uncertainties and low vertical resolution [17–19]. Such spectrometers also poorly cover critical regions for climate change such as the Arctic circle and Boreal forests and cannot investigate day-night cycles. On the other hand, active lidar instruments such as differential absorption lidars offer a better retrieval of greenhouse gas fluxes with greater accuracy and they avoid potential biases due to atmospheric column amounts by providing precise vertical information of greenhouse gas concentrations [20]. They can also provide measurements in dark polar regions to better constrain natural greenhouse gas sources. In addition vertical profiles of clouds and aerosols can be obtained by measuring backscattering coefficients but require *a priori* estimations to calculate aerosol size distributions. Finally conventional spaceborne lidar technology is limited in target gas species and their corresponding laser wavelengths.

To address such shortcomings, spaceborne remote sensing instrumentation could benefit from current advances in the field of laser filamentation and ground-based white-light lidar technology. This paper investigates the optical properties of long distance pulse propagation in the nonlinear regime and addresses the potential of laser filamentation for future spaceborne lidar missions. We present theoretical and numerical investigations of nonlinear optical pulse propagation from 400-km

---

\*Please send correspondence to I. Dicaire or A. Couairon

Email addresses: Isabelle.Dicaire@gmail.com (I. Dicaire), Arnaud.Couairon@polytechnique.fr (A. Couairon)

<sup>1</sup>These authors contributed equally to this work

<sup>2</sup>Present address: Optech Montreal, 1111 Lapierre St., Montreal QC, H8N 2J4, Canada

altitude towards the ground. The structure of the paper is as follows. Section 2 presents an introduction to laser filamentation. Section 3 presents the full numerical model for the simulation of filamentation including the optical Kerr effect, diffraction laws, plasma defocusing, and multiphoton absorption in the presence of various ionising species varying with altitude. Section 4 presents the results of the direct numerical simulations of filamentation from orbit including a detailed analysis of the supercontinuum generated at the collapse point (i.e. at 7.3 km from ground) and beyond. Technical aspects are discussed in section 5 and section 6 concludes with summarising statements and options for future works.

## 2. LASER FILAMENTATION

Laser filamentation, resulting from the nonlinear propagation of intense ultrashort laser pulses in the atmosphere, has become a promising tool in the field of remote sensing of pollutants and bioaerosols. In this technique, powerful femtosecond laser pulses propagate in the atmosphere and can deliver high intensities at altitudes reaching 20 km from the ground. High intensities lead to a competition between various physical effects including the optical Kerr effect focusing the beam and laser energy absorption, which in turn leads to plasma generation and plasma-induced beam defocusing. This competition results in the formation of thin filaments where efficient nonlinear phenomena can be sustained over several tens of meters, among which self-phase modulation leads to the generation of a coherent broadband continuum spanning from ultraviolet to near infrared wavelengths [21]. Filamentation at kilometric distances with ultrashort optical pulses has been demonstrated for vertical propagation from ground to sky [22, 23] and for horizontal propagation [24–26] and white-light lidar measurements have been performed using a single laser source [27–29]. On the other hand, theoretical and numerical investigations of pulse propagation leading to filamentation have been mostly restricted to the regime of laboratory filaments [30] and short scale outdoor filaments [24].

Laser filamentation might offer attractive applications for atmospheric science. For instance it could offer simultaneous range-resolved measurements of key atmospheric trace gas constituents including ozone, nitrogen oxides, bromine oxide, volatile organic compounds, water vapour, carbon dioxide, and methane via absorption bands ranging from the ultraviolet to the near infrared (300nm–3 $\mu$ m). In addition synergistic retrievals of atmospheric pressure and temperature information would be possible via high spectral resolution observations of oxygen (O<sub>2</sub>) lines. Currently such information is obtained via collocated data from weather forecasting models but direct retrievals from oxygen spectral lines is sought in the future [17]. The coherent broadband light continuum generated by the filamentation process is also very attractive for aerosol and cloud characterisation. It could in particular enable direct measurements of relative humidity profile from synergistic observations of oxygen and water vapour lines to improve our understanding of cloud formation and precipitation [31]. It could also lead to a better retrieval of water droplet and aerosol size distribution

and density from multiwavelength backscattering coefficients without providing *a priori* knowledge of the cloud or aerosol properties [31]. Finally filaments in air seem to survive propagation through rain or fog; this apparent robustness is due to the self-healing property of filaments. The surrounding, lower intensity section of the filament establishes an energy flux towards the intense filament core whenever it undergoes losses due to the presence of an obstacle or a strong absorber, playing the role of an energy reservoir. Such property could extend the use of optical wavelengths applications over a broader range of meteorological conditions. In addition, other applications could benefit from the possibility to control the generation of spaceborne laser filaments. For instance, wireless power transportation from space to Earth and directed energy applications based on self-focusing in the atmosphere have been proposed [32].

At sea level, laser filaments are usually generated after an initial self-focusing stage, which requires the beam power to be above a critical threshold. During this stage, the beam diameter shrinks from its initial value to the filament width. This occurs because the beam intensity is higher in the center of the beam, which therefore feels a higher refractive index due to the optical Kerr effect. Similarly to the effect of a focusing lens, this leads to phase curvature accumulation and beam focusing, except that the effect is cumulative and may in principle lead to beam collapse, at finite distance on axis. However the beam intensity just before collapse is sufficiently high so that nonlinear absorption phenomena starts setting in, preventing a catastrophic collapse of the beam and leading to the formation of a filament. Therefore optical beams launched from orbit will form filaments in the atmosphere provided the optical power is high enough and the location of beam collapse is reached before the ground.

It is now well understood that the optical Kerr effect is one of the most important effects in laser filamentation. In order to form a filament, a pulse power  $P$  exceeding a critical threshold ( $P_{cr} \sim 3$  GW in air at ground level) is required. Before forming a filament, the beam undergoes a self-focusing stage over a distance proportional to the diffraction length  $z_R = \pi w_0^2 / \lambda_0^2$ , where  $w_0$  denotes the  $1/e^2$  input beam width and  $\lambda_0$  the laser wavelength, and to the expression  $(P/P_{cr} - 1)^{-1/2}$ . Thus, large beams will form filaments at long distances whereas increasing the pulse power shortens the self-focusing stage. As for generating filaments higher in the atmosphere, laboratory and outdoor experiments have demonstrated filamentation at low gas densities [33–35]. However if gas densities decrease below a certain threshold, the critical power increases above the pulse power, making self-focusing and filamentation impossible.

To investigate the remote generation of laser filamentation from orbital altitudes, state-of-the-art numerical models of laser filamentation were extended to account for the variation of air density with altitude. The model derived for vertical propagation of ultrashort laser pulses consists in a formally similar unidirectional propagation equation [36] and medium response model as those used at sea level. However several coefficients varying with the density of species (oxygen, nitrogen) in air, including the multiphoton absorption coefficient, the plasma absorption cross section, collision time and nonlinear refractive

index, the model was adjusted to reflect those variations. Since the species density enters with different scales for the physical effects considered (plasma induced defocusing and absorption terms), the nonlinear dynamics is not expected to be trivially rescaled with pressure. Therefore, numerical investigations were required to reveal changes in the competition between the nonlinear effects in a realistic atmospheric model.

### 3. SIMULATIONS

#### 3.1. Full numerical model

Our model accounts for the optical Kerr effect, ionisation and plasma effects including nonlinear absorption of energy and plasma defocusing as well as diffraction laws in a stratified atmosphere. The temporal dimension was added to the pulse propagation model (see equation 1), accounting for dispersion in air and spectral broadening due to self-phase modulation. To simulate supercontinuum generation the monochromatic approximation was relaxed, numerically integrating Eq. 1 below.

Our numerical simulations were based on a unidirectional propagation equation along the direction  $z$  for the spectral components  $\hat{E}(\omega, k_x, k_y, z)$  of the electric field envelope  $\mathcal{E}(t, x, y, z)$  of the laser pulse [36]:

$$\partial_z \hat{E} = i \left[ \sqrt{k^2(\omega) - k_\perp^2} - k_0 - k'_0(\omega - \omega_0) \right] \hat{E} + i \frac{\mu_0}{2k(\omega)} (\omega^2 \hat{\mathcal{P}} + i\omega \hat{\mathcal{J}}), \quad (1)$$

where  $\hat{\mathcal{P}}(\omega, k_x, k_y, z)$  and  $\hat{\mathcal{J}}(\omega, k_x, k_y, z)$  denote the Fourier components for the nonlinear polarisation and current sources, which are functions of the electric field and air density. The quantity  $k(\omega) \equiv n(\omega)\omega/c$  denotes the dispersion relation of air [37],  $k_0 \equiv k(\omega_0)$  and  $k'_0 \equiv dk/d\omega|_{\omega_0}$  are taken at the central frequency  $\omega_0$  of the laser. In equation 1, the Fourier transform from time to frequency ( $t \rightarrow \omega$ ) is represented by a hat while a tilde denotes the Fourier transform from space to wavenumbers ( $x, y \rightarrow k_x, k_y$ ) and  $k_\perp^2 \equiv k_x^2 + k_y^2$ . Initial conditions correspond to a Gaussian laser pulse at central wavelength of 800 nm, with initial beam radius  $R_0$ , curvature  $f$ , power  $P$  and full width at half maximum pulse duration  $T_{FWHM}$ :

$$\mathcal{E}(r, t, z_0) = \left( \frac{P}{\pi R_0^2(z)} \right)^{1/2} \exp \left( -\frac{r^2}{2R_0^2} + ik_0 \frac{r^2}{2f} \right) \times \exp \left( -\frac{2 \log 2 t^2}{T_{FWHM}^2} \right), \quad (2)$$

where  $r^2 \equiv x^2 + y^2$ . Details about the medium's response can be found in [Appendix .1](#)

#### 3.2. Atmospheric density model

The response of the medium is described by the laws that link the nonlinear polarisation and the current to the electric field envelope. Embedded in the medium's response to laser beam propagation is the dependence on gas species and their densities. The atmospheric density profiles were taken from

the NRLMSISE-00 empirical and global model of the Earth's atmosphere from ground to thermospheric heights freely available on the Community Coordinated Modeling Center (CCMC) online platform [38]. The initial model database derived from ground, rockets and satellite-based measurements has been extended on two occasions to include incoherent scatter radar and mass spectrometer data (1990) as well as drag on satellites and other space objects (2001) [38]. Below 72.5 km, the model is primarily based on the Middle Atmosphere Program (MAP) Handbook [39] giving tabulated values for zonal average temperature and pressure, supplemented with data from the National Meteorological Center below 20 km. Given the geographic coordinates, the date and the time of the day, the model calculates vertical profiles of neutral temperature, densities of He, O, O<sub>2</sub>, N, N<sub>2</sub>, Ar, H as well as total air mass density.

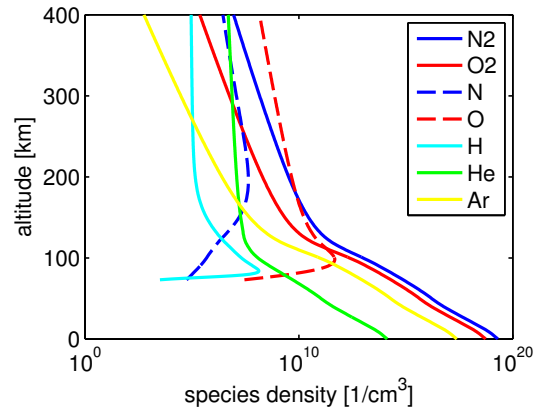


Figure 1: Species density dependence on height retrieved via MSIS-class model.

The model provides excellent average values for each atmospheric layer from 400-km altitude to ground level; it is thus well suited for the current study. The species density profiles shown in Fig. 1 correspond to values averaged over several day and night records taken during Spring 2014 above Western Europe. Molecular nitrogen and oxygen are the dominant species between sea level and 120 km and were therefore implemented in the medium's response model. Contributions of all other species to the generated plasma were negligible.

### 4. RESULTS

Results show the generation of a very broad supercontinuum at 7.3 km altitude collocated with pulse splitting and beam collapse. Simulations were initiated with a Gaussian pulse of 500-fs duration. This value is optimum for numerical simulations of filamentation from orbit as it ensures an optimal trade-off between dispersion up to the collapse point and modulation instability during filamentation. Short pulses would tend to postpone the collapse point by decreasing the peak intensity via pulse broadening induced by group velocity dispersion. Long pulses propagating over large distances would undergo modulation instability and pulse splitting. The pulse duration was chosen to keep both of these effects negligible.

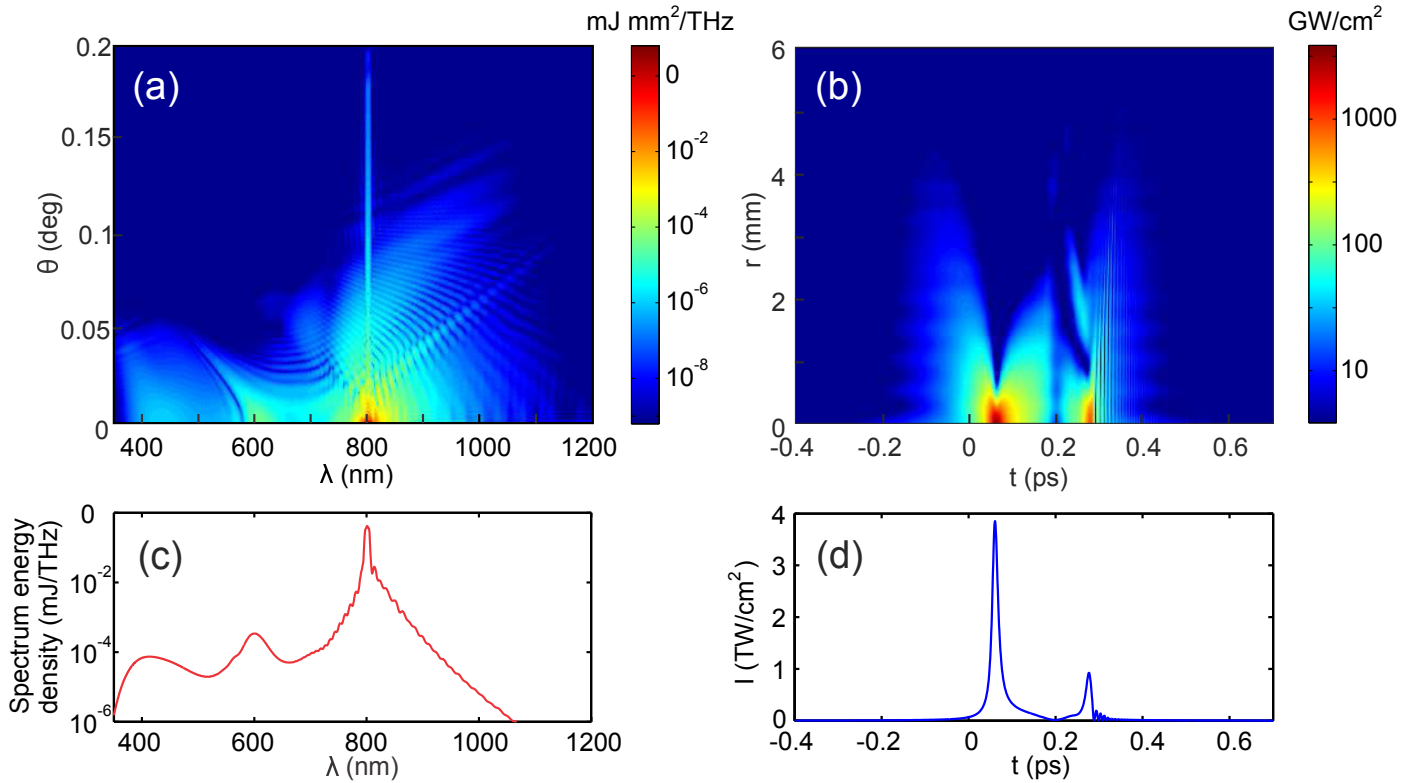


Figure 2: (a) Angle-resolved supercontinuum spectrum generated by filamentation, at 7.3 km from the earth, while (c) depicts the spectrum integrated over transverse wavenumbers (or angles). (b) Spatio-temporal intensity profile and (d) axial intensity profile of the pulse at  $z = 7.3$  km. Initial conditions: Input beam radius  $R_0 = 50$  cm, pulse duration  $T_{\text{FWHM}} = 500$  fs, initial beam peak power  $P = 45 P_{cr,0}^* = 143$  GW and pulse energy 76 mJ.

Results are depicted in figures 2 – 3 for a 76-mJ pulse energy. Figure 2 shows the spectral content of the pulse undergoing filamentation at an altitude of 7.3 km, together with the spatio-temporal intensity distribution. In addition to the axial ( $\theta = 0$ ) supercontinuum with high power density close to the pump wavelength ( $\lambda_0 = 800$  nm), we also recognise conical emission, a manifestation of angular dispersion, from the high intensity branches indicating that different frequencies propagate at different angles. The spectral region around these branches is populated because of the incident laser pulse scattering off nonlinear polarisation waves (the medium’s response) [40]. In all dispersive media, this scattering process results in the generation of conical branches in  $(\theta-\lambda)$  spectra, also called X-waves [41], the skeleton of which is determined by a phase-matching condition between the laser pulse, the nonlinear polarisation wave and the scattered wave [40–42]. The integrated spectrum in Fig. 2(c) shows that the supercontinuum is smooth and spans from 350 nm to 1.1  $\mu\text{m}$ . Besides the main peak at 800 nm, the spectrum shows secondary peaks at 400 and 600 nm at the intersection of the conical branches with the propagation axis ( $\theta = 0$ ). Each of these peaks reflects the space-time dynamics of the pulse undergoing filamentation. Both peaks are generated by the trailing split pulse shown in Fig. 2(d), which is responsible for the excitation of nonlinear polarisation waves. The velocity of the polarisation waves determines phase-matching conditions and the preferential region where the  $(\theta-\lambda)$  spectrum

is populated, which in turn determines the position of the spectral peaks in the integrated spectrum. The spatio-temporal intensity distribution shown in Fig. 2(b) illustrates that the pulse splitting phenomenon actually follows from a severe pulse re-shaping involving space-time couplings.

Figure 3(a) shows how the integrated spectrum is populated as a function of altitude, which decreases along pulse propagation. The spectrum remains narrow until the nonlinear focus where a very quick broadening occurs. The supercontinuum reflects the formation of an intense and short trailing pulse as displayed in Fig. 3(b). The fluence change with altitude in Fig. 3(c) shows beam focusing at 7.312-km altitude corresponding to the supercontinuum generation point. As it can be seen the filament radius shrinks to less than 200  $\mu\text{m}$  and the high intensity (20  $\text{TW}/\text{cm}^2$ ) is sustained over  $\sim 2$  m after the nonlinear focus. This intensity is consistent with measurements of the clamping intensity for filamentation in air at ground level, which ranges from 10 to 100  $\text{TW}/\text{cm}^2$  [43–45]. Although it should be quasi-independent of pressure [34, 35], we find a slightly lower peak intensity than the ground level clamping intensity for filaments at high altitude, in keeping with their larger filament width and longer pulse duration after dispersion in the troposphere.

A secondary peak in the spectrum appears at 7.305-km altitude, which is connected to small refocusing of the pulse visible in Fig. 3(b). However, its intensity is too low to generate a significant plasma density, although the beam keeps propagating in

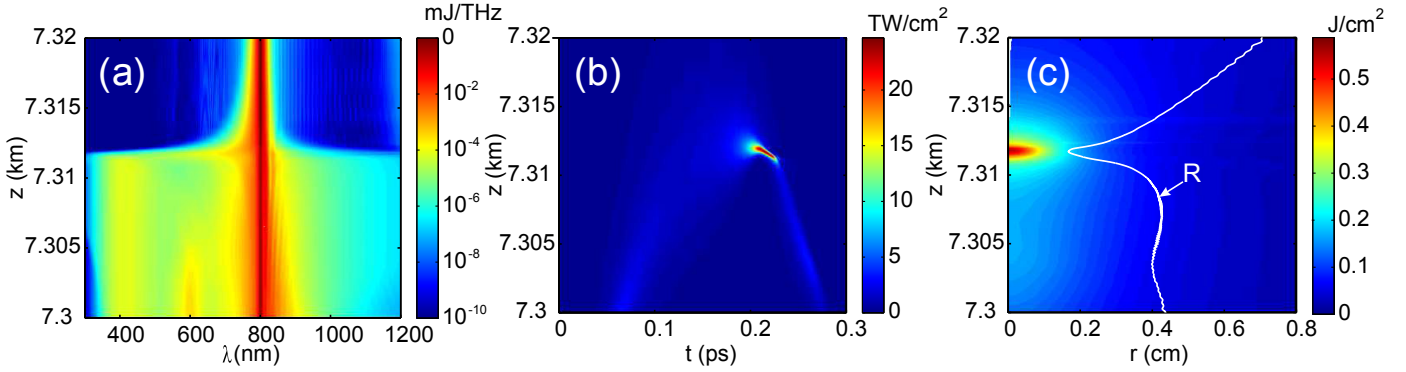


Figure 3: (a) Angle-integrated supercontinuum spectrum (in logarithmic scale), (b) axial pulse profile and (c) beam fluence vs altitude close to the nonlinear focus. The white line in panel (c) depicts the beam radius evolution.

the form of an intense light tube of radius  $\sim 400 \mu\text{m}$ . The supercontinuum spectrum is generated at the beginning of the 10-m long filament where its intensity reaches up to  $20 \text{ TW/cm}^2$ , in the first meters after the nonlinear focus. The supercontinuum expands rapidly then does not broaden further from the nonlinear focus. As seen in Fig. 2(a), the white-light continuum is mostly emitted in the forward direction. Further propagation of the white-light continuum towards the ground will lead to forward and backward scattering by atmospheric species, the latter of which can be collected and analysed by a receiving unit and time-resolved spectrometer on board a spacecraft to perform range-resolved spectroscopic measurements.

## 5. DISCUSSION

The technical aspects of generating such beams in orbit are hereby considered, starting from the terrestrial mobile laser system and taking into account recent advances in space-qualification of optical components and optical standoff detection schemes. The first terrestrial mobile femtosecond-terawatt laser and detection system was presented in 2002 [46]. It consisted of a compact Ti:Sapphire oscillator and a Nd:YAG pumped Ti:Sapphire amplification chain including a regenerative amplifier and two 4-pass amplifiers. It was fitted in a standard ISO 20 ft container and had a total mass of 10000 kg, including laser source, detection system, power supplies and heat exchanger. Consuming 30 kW, it produced 350 mJ 70 fs pulses with peak power of 5 TW at a repetition rate of 10 Hz. Notable advancements have been realised, as the latest mobile laser systems are now capable of producing up to 300 mJ 40 fs pulses, consuming only 10 kW and with a mass of only 1400 kg, contained within a volume of  $1.5 \times 3 \times 1.9 \text{ m}$  [47]. Such system parameters would be sufficient to remotely generate the filaments presented in this paper.

Compared to ground-based systems, space-based designs specifically require to be lightweight, compact, energy efficient and not cause electromagnetic interference. Further improvements in mass, volume and efficiency compared to latest ground systems seem possible, though space qualification would likely also introduce additional mass and complexity due

to e.g. different heat-rejection systems, redundancy, reliability and optical bench requirements. For comparison, the Atmospheric Laser Doppler Instrument (ALADIN) hosting a 355-nm Nd:YAG laser on-board the ADM-Aeolus spacecraft scheduled for launch in 2015 requires 1.4 kW, has a payload mass of 450 kg on-board a 650 kg platform [48, 49].

Substantial R&D efforts were made to space-qualify high power lasers since the mid-1990s [50–53]. Space qualification has proven challenging and lengthy, with special efforts made for maintaining precision alignments of optical mounts during and after launch, preventing contamination of optics from out-gassing materials in vacuum, resistance of electronic components and optical materials to vacuum, thermal cycling, and radiation exposure [50, 53]. Achieving good coating performance under vacuum is also challenging, with strong laser degradation for porous coatings under vacuum exposure [54]. To avoid vacuum-related degradation, laser heads tend to be mounted in hermetically sealed boxes filled with synthetic air at atmospheric pressure [55]. To avoid temperature gradients, heat-dissipating elements such as laser diodes and electronics are mounted on a thermally conductive metal alloy structure [55]. Finally, the next generation of space lasers might come from the fibre optics field, offering high efficiency, compactness, alignment insensitivity and gain bandwidth amongst other things [56]. The first launch and operation of a fibre-based femtosecond oscillator has been reported in 2014 on a 100 kg class Korean satellite (STSAT-2C) [57]. At higher power levels, ongoing efforts have been reported regarding the design and development of phased-array femtosecond fibre lasers based on coherent amplification networks [56, 58]. The successful development and space qualification of femtosecond laser systems is expected to enable a large range of space applications such as laser debris removal, optical free space communications, wireless power transfer, and high-precision frequency comb metrology [32, 57].

As for the detection system, the terrestrial teramobile system includes a receiving telescope, three diffraction gratings, as well as several detectors covering the supercontinuum spectrum [46] to measure the backscattered signal. Charge-coupled devices (CCDs), photomultiplier tubes (PMTs) and avalanche

photodiodes (APDs) were integrated into the detection unit.

Scaling the teramobile system to an Earth-orbiting platform will require a much larger lidar power-area product due to the longer propagation distance and instrument velocity. One can expect that larger telescope diameters and state-of-the-art detection techniques will be required to adapt the system to orbiting altitudes. As an example the Aeolus Doppler lidar instrument will host a 1.5 m Cassegrain telescope, a dual-channel receiver with an Accumulation Charge Coupled Device (ACCD) with on-chip signal averaging for noise reduction. It will obtain particle backscatter and extinction coefficients up to an altitude of 30 km with an overall uncertainty of 10%-15% and 15%-30%, respectively, based on several lidar validation campaigns including the Lidar-in-space Technology Experiment (LITE) [59] and numerous observation missions on board aircraft platforms [60].

For the currently-envisaged space-based version of femtosecond teramobile lidar, adapting the system to an Earth-orbiting platform would require a dedicated space system study, taking into account the backscattering coefficient of the forward-emitted white-light continuum. The latter, combined with the telescope diameter, will impact the amount of light collected on board the spacecraft and the detector requirements. For completeness, we include some notable advancements of receiver systems. To help enhance the signal-to-noise ratio (SNR) of the backscattered light, the detection technique could benefit from recently proposed optical stand-off detection schemes relying on laser filamentation [61]. For instance, SNR improvements as large as  $10^4$  could be obtained for stand-off distances of 100 m via filament-generated air waveguides [62]. The on-board detection system could also benefit from recent developments of electron-multiplying CCDs (EMCCDs), which have enabled a new generation of detectors with low readout noise and high quantum efficiency [63]. Issues during space-qualification were the device tolerance to radiation, charge transfer efficiency at low signal levels and gain degradation at the multiplication register [64, 65]. A successful space qualification of EMCCDs could provide attractive solutions for space borne lidar applications due to their narrow sampling windows and low crosstalk between successive samples [64, 66]. Overall the preliminary analysis of the general parameters and technologies required to initiate filamentation from orbital altitudes using a space-based femtosecond laser source and spectrometer detection system has not identified any show-stoppers or critical issues that could prevent its realisation.

## 6. CONCLUSIONS

In this study we investigated the remote generation of filamentation from orbital altitudes. Propagation in the stratified atmosphere was taken into account via an air density profile varying with molecule type and distance from the ground. Our results indicate that laser filamentation and remote supercontinuum generation from space is possible based on direct simulations of nonlinear unidirectional pulse propagation equations. Our results have also shown that laser filamentation can lead to the remote generation of a supercontinuum in the atmosphere

extending from 350 nm to 1.1  $\mu\text{m}$ , collocated with pulse splitting and beam collapse at an altitude of 7.3 km.

This work constitutes a theoretical proof-of-concept of laser filamentation and remote supercontinuum generation from orbital altitudes. This work might provide the basis for a new remote sensing tool for atmospheric research: an Earth-orbiting white-light lidar. It would enable the global monitoring of various atmospheric constituents including trace gases and aerosols at various atmospheric depths from a single femtosecond laser source on-board a spacecraft platform. These findings provide a solid theoretical basis for an application study, e.g. for white-light atmospheric remote sensing, as well as for a detailed system-level study of a spacecraft payload based on laser filamentation, starting from the tested ground system and taking into account recent developments in femtosecond fibre lasers, detection units and optical stand-off detection schemes to conceive the spaceborne system.

## 7. REFERENCES

- [1] M. Berger, J. Moreno, J. A. Johannessen, P. F. Levelt, and R. F. Hanssen. Esa's sentinel missions in support of earth system science. *Remote Sensing of Environment*, 120(0):84 – 90, 2012. ISSN 0034-4257. The Sentinel Missions - New Opportunities for Science.
- [2] C. S. partners. Climate and clean air coalition annual report, 2014.
- [3] K. R. Smith, M. Jerrett, H. R. Anderson, R. T. Burnett, V. Stone, R. Derwent, R. W. Atkinson, A. Cohen, S. B. Shonkoff, D. Krewski, et al. Public health benefits of strategies to reduce greenhouse-gas emissions: health implications of short-lived greenhouse pollutants. *The Lancet*, 374(9707): 2091–2103, 2010.
- [4] D. Fowler. *Ground-level ozone in the 21st century: future trends, impacts and policy implications*. Royal Society, 2008.
- [5] D. S. Stevenson, F. J. Dentener, M. G. Schultz, K. Ellingsen, T. P. C. van Noije, O. Wild, G. Zeng, M. Amann, C. S. Atherton, N. Bell, D. J. Bergmann, I. Bey, T. Butler, J. Cofala, W. J. Collins, R. G. Derwent, R. M. Doherty, J. Drevet, H. J. Eskes, A. M. Fiore, M. Gauss, D. A. Hauglustaine, L. W. Horowitz, I. S. A. Isaksen, M. C. Krol, J.-F. Lamarque, M. G. Lawrence, V. Montanaro, J.-F. Miller, G. Pitari, M. J. Prather, J. A. Pyle, S. Rast, J. M. Rodriguez, M. G. Sanderson, N. H. Savage, D. T. Shindell, S. E. Strahan, K. Sudo, and S. Szopa. Multimodel ensemble simulations of present-day and near-future tropospheric ozone. *Journal of Geophysical Research: Atmospheres*, 111(D8):D08301, 2006.
- [6] J. Lelieveld, F. Dentener, W. Peters, and M. Krol. On the role of hydroxyl radicals in the self-cleansing capacity of the troposphere. *Atmospheric Chemistry and Physics*, 4(9/10):2337–2344, 2004.
- [7] J. E. Penner, M. J. Prather, I. S. Isaksen, J. S. Fuglestedt, Z. Klimont, and D. S. Stevenson. Short-lived uncertainty? *Nature Geoscience*, 3(9): 587–588, 2010.
- [8] B. J. Bloomer, J. W. Stehr, C. A. Piety, R. J. Salawitch, and R. R. Dickerson. Observed relationships of ozone air pollution with temperature and emissions. *Geophysical Research Letters*, 36(9), 2009.
- [9] Y. Kasai, K. Kita, Y. Kanaya, A. M. Team, et al. The japanese air pollution observation missions, gmap-asia and apollo. In *AGU Fall Meeting Abstracts*, volume 1, page 03, 2011.
- [10] J. Rogelj, M. Schaeffer, M. Meinshausen, D. T. Shindell, W. Hare, Z. Klimont, G. J. M. Velders, M. Amann, and H. J. Schellnhuber. Disentangling the effects of co2 and short-lived climate forcer mitigation. *Proceedings of the National Academy of Sciences*, 2014.
- [11] H. Bovensmann, J. Burrows, M. Buchwitz, J. Frerick, S. Noël, V. Rozanov, K. Chance, and A. Goede. Sciamachy: Mission objectives and measurement modes. *Journal of the Atmospheric Sciences*, 56(2): 127–150, 1999.
- [12] A. Butz, S. Guerlet, O. Hasekamp, D. Schepers, A. Galli, I. Aben, C. Frankenberg, J.-M. Hartmann, H. Tran, A. Kuze, et al. Toward accurate co2 and ch4 observations from gosat. *Geophysical Research Letters*, 38(14), 2011.

- [13] H. Boesch, D. Baker, B. Connor, D. Crisp, and C. Miller. Global characterization of  $\text{CO}_2$  column retrievals from shortwave-infrared satellite observations of the orbiting carbon observatory-2 mission. *Remote Sensing*, 3(2):270–304, 2011.
- [14] M. Buchwitz, M. Reuter, H. Bovensmann, D. Pillai, J. Heymann, O. Schneising, V. Rozanov, T. Krings, J. P. Burrows, H. Boesch, C. Gerbig, Y. Meijer, and A. Löscher. Carbon monitoring satellite (carbonsat): assessment of scattering related atmospheric  $\text{CO}_2$  and  $\text{CH}_4$  retrieval errors and first results on implications for inferring city  $\text{CO}_2$  emissions. *Atmospheric Measurement Techniques Discussions*, 6(3):4769–4850, 2013.
- [15] V. A. Velazco, M. Buchwitz, H. Bovensmann, M. Reuter, O. Schneising, J. Heymann, T. Krings, K. Gerilowski, and J. P. Burrows. Towards space based verification of  $\text{CO}_2$  emissions from strong localized sources: fossil fuel power plant emissions as seen by a carbonsat constellation. *Atmospheric Measurement Techniques*, 4(12):2809–2822, 2011.
- [16] J. Callies, E. Corpaccioli, M. Eisinger, A. Hahne, and A. Lefebvre. Gome-2-metop’s second-generation sensor for operational ozone monitoring. *ESA bulletin*, 102:28–36, 2000.
- [17] S. Noël, K. Bramstedt, A. Rozanov, H. Bovensmann, and J. Burrows. Stratospheric methane profiles from sciamachy solar occultation measurements derived with onion peeling doas. *Atmospheric Measurement Techniques Discussions*, 4(4):4801–4823, 2011.
- [18] A. Rozanov, S. Köhl, A. Doicu, C. McLinden, J. Pučkite, H. Bovensmann, J. Burrows, T. Deutschmann, M. Dorf, F. Goutail, et al. Bro vertical distributions from sciamachy limb measurements: comparison of algorithms and retrieval results. *Atmospheric Measurement Techniques*, 4(7):1319–1359, 2011.
- [19] J. Meyer, A. Bracher, A. Rozanov, A. Schlesier, H. Bovensmann, and J. Burrows. Solar occultation with sciamachy: algorithm description and first validation. *Atmospheric Chemistry and Physics*, 5(6):1589–1604, 2005.
- [20] C. Kiemle, M. Quatrevalet, G. Ehret, A. Amediek, A. Fix, and M. Wirth. Sensitivity studies for a space-based methane lidar mission. *Atmospheric Measurement Techniques Discussions*, 4(3):3545–3592, 2011.
- [21] J. Kasparian, M. Rodriguez, G. Méjean, J. Yu, E. Salmon, H. Wille, R. Bourayou, S. Frey, Y.-B. André, A. Mysyrowicz, R. Sauerbrey, J.-P. Wolf, and L. Wöste. White light filaments for atmospheric analysis. *Science*, 301:61–64, 2003.
- [22] L. Wöste, C. Wedekind, H. Wille, P. Rairoux, B. Stein, S. Nikolov, C. Werner, S. Niedermeier, F. Ronneberger, H. Schillinger, and R. Sauerbrey. Femtosecond atmospheric lamp. *Laser und Optoelektronik*, 29(5):51–53, 1997.
- [23] M. Rodriguez, R. Bourayou, G. Méjean, J. Kasparian, J. Yu, E. Salmon, A. Scholz, B. Stecklum, J. Eislöffel, U. Laux, A. P. Hatzes, R. Sauerbrey, L. Wöste, and J.-P. Wolf. Kilometer-range nonlinear propagation of femtosecond laser pulses. *Phys. Rev. E*, 69:036607, 2004.
- [24] G. Méchain, A. Couairon, Y.-B. André, C. D’Amico, M. Franco, B. Prade, S. Tzortzakis, A. Mysyrowicz, and R. Sauerbrey. Long range self-channeling of infrared laser pulses in air: a new propagation regime without ionization. *Appl. Phys. B*, 79:379–382, 2004.
- [25] G. Méchain, C. D’Amico, Y.-B. André, S. Tzortzakis, M. Franco, B. Prade, A. Mysyrowicz, A. Couairon, E. Salmon, and R. Sauerbrey. Range of plasma filaments created in air by a multiterawatt femtosecond laser. *Optics Commun.*, 247:171–180, 2005.
- [26] M. Durand, A. Houard, B. Prade, A. Mysyrowicz, A. Durécu, B. Moreau, D. Fleury, O. Vasseur, H. Borchert, K. Diener, R. Schmitt, F. Théberge, M. Chateaufneuf, J.-F. Daigle, and J. Dubois. Kilometer range filamentation. *Opt. Express*, 21(22):26836–26845, Nov 2013.
- [27] G. Méjean, J. Kasparian, E. Salmon, J. Yu, J.-P. Wolf, R. Bourayou, R. Sauerbrey, M. Rodriguez, L. Wöste, H. Lehmann, B. Stecklum, U. Laux, J. Eislöffel, A. Scholz, and A. P. Hatzes. Towards a supercontinuum-based infrared lidar. *Appl. Phys. B*, 77(2-3):357 – 359, 2003.
- [28] G. Méjean, J. Kasparian, J. Yu, S. Frey, E. Salmon, and J.-P. Wolf. Remote detection and identification of biological aerosols using a femtosecond terawatt lidar system. *Appl. Phys. B*, 78(5):535 – 537, 2004.
- [29] O. A. Bukin, M. Y. Babii, S. S. Golik, A. A. Il’in, A. M. Kabanov, A. V. Kolesnikov, Y. N. Kulchin, V. V. Lisitsa, G. G. Matvienko, V. K. Oshlakov, and K. A. Shmirko. Lidar sensing of the atmosphere with gigawatt laser pulses of femtosecond duration. *Quantum Electronics*, 44(6):563, 2014.
- [30] A. Couairon and A. Mysyrowicz. Femtosecond filamentation in transparent media. *Phys. Rep.*, 441(2):47–189, 2007.
- [31] R. Bourayou, G. Méjean, J. Kasparian, M. Rodriguez, E. Salmon, J. Yu, H. Lehmann, B. Stecklum, U. Laux, J. Eislöffel, et al. White-light filaments for multiparameter analysis of cloud microphysics. *J. Opt. Soc. Am. B*, 22(2):369–377, 2005.
- [32] A. M. Rubenchik, M. P. Fedoruk, and S. K. Turitsyn. Laser beam self-focusing in the atmosphere. *Phys. Rev. Lett.*, 102(23):233902, 2009.
- [33] G. Méchain, G. Méjean, R. Ackermann, P. Rohwetter, Y.-B. André, J. Kasparian, B. Prade, K. Stelmaszczyk, J. Yu, E. Salmon, W. Winn, L. A. V. Schlie, A. Mysyrowicz, R. Sauerbrey, L. Wöste, and J.-P. Wolf. Propagation of fs-TW laser filaments in adverse atmospheric conditions. *Appl. Phys. B*, 80:785–789, 2005.
- [34] A. Couairon, M. Franco, G. Méchain, T. Olivier, B. Prade, and A. Mysyrowicz. Femtosecond filamentation in air at low pressures: Part I: Theory and numerical simulations. *Opt. Commun.*, 259:265–273, 2006.
- [35] G. Méchain, T. Olivier, M. Franco, A. Couairon, B. Prade, and A. Mysyrowicz. Femtosecond filamentation in air at low pressures: Part II: Laboratory experiments. *Optics Commun.*, 261:322–326, 2006.
- [36] A. Couairon, E. Brambilla, T. Corti, D. Majus, O. de J. Ramírez-Góngora, and M. Kolesik. Practitioners guide to laser pulse propagation models and simulation. *Eur. Phys. J. Special Topics*, 199:5–76, 2011.
- [37] E. R. Peck and K. Reeder. Dispersion of air. *J. Opt. Soc. Am.*, 62(8):958–962, Aug 1972.
- [38] J. M. Picone, A. E. Hedin, D. P. Drob, and A. C. Aikin. NRLMSISE-00 empirical model of the atmosphere: Statistical comparisons and scientific issues. *J. of Geophys. Res.: Space Physics*, 107(A12):SIA 15–1–SIA 15–16. ISSN 2156-2202.
- [39] K. Labitzke, J. J. Barnett, and B. Edwards, editors. *Middle Atmosphere Program. Handbook for MAP*, volume 16. SCOSTEP, University of Illinois, Urbana, 1985.
- [40] M. Kolesik, E. M. Wright, and J. V. Moloney. Interpretation of the spectrally resolved far field of femtosecond pulses propagating in bulk nonlinear dispersive media. *Opt. Express*, 13(26):10729–10741, Dec 2005.
- [41] D. Faccio, M. Porras, A. Dubietis, F. Bragheri, A. Couairon, and P. Di Trapani. Conical emission, pulse splitting and X-wave parametric amplification in nonlinear dynamics of ultrashort light pulses. *Phys. Rev. Lett.*, 96:193901, 2006.
- [42] M. Durand, K. Lim, V. Jukna, E. McKee, M. Baudelet, A. Houard, M. Richardson, A. Mysyrowicz, and A. Couairon. Blueshifted continuum peaks from filamentation in the anomalous dispersion regime. *Phys. Rev. A*, 87:043820, 2013.
- [43] S. I. Mitryukovskiy, Y. Liu, A. Houard, and A. Mysyrowicz. Re-evaluation of the peak intensity inside a femtosecond laser filament in air. *J. Phys. B: At. Mol. Opt. Phys.*, 48:094003, 2015.
- [44] S. Xu, X. Sun, B. Zeng, W. Chu, J. Zhao, W. Lei, Y. Cheng, Z. X. Z, and S. Chin. Simple method of measuring laser peak intensity inside femtosecond laser filament in air. *Opt. Express*, 20:299–307, 2012.
- [45] X. Sun, S. Xu, J. Zhao, W. Liu, Y. Cheng, Z. Xu, S. Chin, and G. Mu. Impressive laser intensity increase at the trailing stage of femtosecond laser filamentation in air. *Opt. Express*, 20:4790, 2013.
- [46] H. Wille, M. Rodríguez, J. Kasparian, D. Mondelain, J. Yu, A. Mysyrowicz, R. Sauerbrey, J.-P. Wolf, and L. Wöste. Teramobile: A mobile femtosecond-terawatt laser and detection system. *Eur. Phys. J.-Appl. Phys.*, 20(03):183–190, 2002.
- [47] Amplitude Technologies. TT-MOBILE: Integrated mobile laser system for filamentation in air. Technical report, 2014 (Accessed: 5th March 2015). URL <http://www.amplitude-technologies.com/>.
- [48] A. Cosentino, A. D’Ottavi, A. Sapia, and E. Suetta. Spaceborne lasers development for aladin and atlid instruments. In *Geoscience and Remote Sensing Symposium (IGARSS), 2012 IEEE International*, pages 5673–5676, July 2012.
- [49] P. Ingmann and M. Endemann. ADM-Aeolus ESA’s wind mission. Technical Report R-236, European Space Agency, ESTEC, Noordwijk, The Netherlands, 2005. URL <http://www.esa.int/esapub/br/br236/br236.pdf>.
- [50] Y. Lien, E. Reinhold, D. Wernham, M. Endemann, M. Jost, E. Armandillo, W. Riede, H. Schroeder, and P. Allenspacher. Risk mitigation in spaceborne lasers. *Proc. SPIE*, 6182:618202–618202–9, 2006.
- [51] G. J. Komar. Active optical technology: recent developments and lessons learned. *Proc. SPIE*, 8159:815902–815902–7, 2011.

- [52] M. Zahir and Y. Durand. Critical laser technology developments and ESA space qualification approach in support of ESA's Earth observation missions. *Proc. SPIE*, 8159:815904–815904–15, 2011.
- [53] M. Lieber, M. Adkins, R. Pierce, R. Warden, C. Wallace, and C. Weimer. Frequency stabilized lasers for space applications. *Proc. SPIE*, 9226:922605–922605–15, 2014.
- [54] W. Riede, P. Allenspacher, M. Lammers, D. Wernham, A. Ciapponi, C. Heese, L. Jensen, H. Maedebach, S. Schrameyer, and D. Ristau. From ground to space: how to increase the confidence level in your flight optics. *Proc. SPIE*, 8885:88850D–88850D–9, 2013.
- [55] R. Kallenbach, E. Murphy, B. Gramkow, M. Rech, K. Weidlich, T. Leikert, R. Henkelmann, B. Trefzger, B. Metz, H. Michaelis, K. Lingenauber, S. DelTogno, T. Behnke, N. Thomas, D. Piazza, and K. Seiferlin. Space-qualified laser system for the bepicolombo laser altimeter. *Appl. Opt.*, 52(36):8732–8746, Dec 2013.
- [56] R. Souillard, M. N. Quinn, and G. Mourou. Design and properties of a coherent amplifying network laser. *Applied Optics*, 54(15):4640–4645, 2015.
- [57] J. Lee, K. Lee, Y.-S. Jang, H. Jang, S. Han, S.-H. Lee, K.-I. Kang, C.-W. Lim, Y.-J. Kim, and S.-W. Kim. Testing of a femtosecond pulse laser in outer space. *Sci. Rep.*, 4, 2014.
- [58] G. Mourou, B. Brocklesby, T. Tajima, and J. Limpert. The future is fibre accelerators. *Nature Photonics*, 7(4):258–261, 2013.
- [59] D. M. Winker, R. H. Couch, and M. P. McCormick. An overview of lite: Nasa's lidar in-space technology experiment. *Proceedings of the IEEE*, 84(2):164–180, 1996.
- [60] A. Ansmann, U. Wandinger, O. L. Rille, D. Lajas, and A. G. Straume. Particle backscatter and extinction profiling with the spaceborne high-spectral-resolution doppler lidar aladin: methodology and simulations. *Appl. Opt.*, 46(26):6606–6622, Sep 2007.
- [61] N. Jhajj, J. Wahlstrand, and H. Milchberg. Optical mode structure of the air waveguide. *Opt. Lett.*, 39(21):6312–6315, 2014.
- [62] E. W. Rosenthal, N. Jhajj, J. K. Wahlstrand, and H. M. Milchberg. Collection of remote optical signals by air waveguides. *Optica*, 1:5–9, 2014.
- [63] O. Djazovski, O. Daigle, D. Laurin, M. Bedirian, M.-E. Ducharme, É. Artigau, and R. Doyon. Electron-multiplying ccds for future space instruments. *Proc. SPIE*, 8915:89150Q–89150Q–13, 2013.
- [64] D. R. Smith, D. M. Walton, R. Ingle, A. D. Holland, M. Cropper, and P. Pool. EMCCDs for space applications. *Proc. SPIE*, 6276:62760K–62760K–12, 2006. doi: 10.1117/12.671368.
- [65] D. R. Smith, R. Ingle, and A. D. Holland. Proton Irradiation of EMCCDs. *IEEE Transactions on Electron Devices*, 53:205–210, February 2006.
- [66] B. De Monte and R. T. Bell. Development of an EMCCD for LIDAR applications. *Proc. SPIE*, 7419:74190Q–74190Q–7, 2009.

### Appendix .1. MEDIUM'S RESPONSE MODEL

The response of the medium is described by the relations linking the nonlinear polarisation  $\mathcal{P}(t, x, y, z)$  and the current  $\mathcal{J}(t, x, y, z)$  to the electric field envelope. Our model accounts for the optical Kerr effect, ionisation and plasma effects including nonlinear absorption of energy and plasma defocusing. These phenomena are described by the set of equations (.1–.6),

referred to as the medium's response model:

$$\mathcal{P} = 2\epsilon_0 n_0 n_2 \mathcal{I} \mathcal{E}, \quad (.1)$$

$$\mathcal{J} = \epsilon_0 n_0 c \sum_s (\sigma_s \rho_e + \beta_{K_s} \mathcal{I}^{K_s-1}) (1 - \frac{\rho_{s^+}}{\rho_{s,b}}) \mathcal{E} \quad (.2)$$

$$+ i \epsilon_0 \omega_0 \frac{\rho_e}{\rho_{cr}} \mathcal{E} \quad (.3)$$

$$\frac{\partial \rho_{s^+}}{\partial t} = (\sigma_{K_s} \mathcal{I}^{K_s} \rho_{s,b} + \frac{\sigma_s \mathcal{I}}{U_{i,s}} \rho_e) (1 - \frac{\rho_{s^+}}{\rho_{s,b}}) \quad (.4)$$

$$\rho_{s^+} = \rho_{s,b}(z) - \rho_s \quad (.5)$$

$$\rho_e = \sum_s \rho_{s^+} \quad (.6)$$

The quantity  $\mathcal{I} \equiv \epsilon_0 n_0 c |\mathcal{E}|^2 / 2$  denotes the pulse intensity and  $n_2$  denotes the nonlinear index coefficient. The quantities  $\rho_{s,b}(z)$ ,  $\rho_s(t, x, y, z)$ ,  $\rho_{s^+}(t, x, y, z)$  and  $\rho_e(t, x, y, z)$  denote the background density of species  $s$  (nitrogen  $N_2$ , oxygen  $O_2$ , etc), the density of neutral atomic (Ar, N, O) or molecular ( $N_2$ ,  $O_2$ ) species  $s$ , ions  $s^+$  generated by single ionisation, and electrons, respectively. The density  $\rho_{cr} \equiv \epsilon_0 m_e \omega_0^2 / e^2$  denotes the critical plasma density beyond which the plasma becomes opaque to the wave of frequency  $\omega_0$ . The quantity  $K_s \equiv \langle \frac{U_{i,s}}{\hbar \omega_0} + 1 \rangle$ , where brackets mean the integer part, denotes the number of photons necessary for an atom or molecule with ionisation potential  $U_{i,s}$  to liberate an electron by multiphoton ionisation, with rate coefficient  $\sigma_{K_s}$ . The corresponding multiphoton absorption coefficient  $\beta_{K_s}(z) \equiv \sigma_{K_s} K_s \hbar \omega_0 \rho_{s,b}(z)$  and the plasma absorption cross section  $\sigma_s(z) \equiv (\tau_{c,s}(z) n_0 c \rho_{cr})^{-1}$  are both proportional to the background density of  $s$  species,  $\rho_{s,b}(z)$ , before the pulse. The parameters  $n_2$ ,  $\beta_{K_s}$ ,  $\sigma_s$  and the collision time  $\tau_{c,s}$  thus all depend on altitude whereas other parameters ( $U_{i,s}$ ,  $K_s$ ,  $\sigma_{K_s}$ ,  $\rho_{cr}$ ) are constant.

Reference values for all parameters can be found in tables 1&2 below.

Table .2: Parameters for air at ground level

Parameter	Value
$\lambda_0$ [nm]	800
$n_0$	1.0
$n_{2,0}$ [cm <sup>2</sup> /W]	$3 \times 10^{-19}$
$\rho_{\text{air},0}$ [cm <sup>-3</sup> ]	$2.5 \times 10^{19}$

Table .1: Material parameters for each species at ground level

Species $s$	$O_2$	$N_2$	Ar
$\rho_{s,b,0}$ [cm <sup>-3</sup> ]	$5.25 \times 10^{18}$	$1.96 \times 10^{19}$	$2.33 \times 10^{17}$
$U_{i,s}$ [eV]	12.063	15.576	15.759
$K_s$	8	11	11
$\sigma_{K_{s,s}}$ [s <sup>-1</sup> cm <sup>2K<sub>s</sub></sup> W <sup>-K<sub>s</sub></sup> ]	$3.6 \times 10^{-96}$	$7.5 \times 10^{-140}$	$6.0 \times 10^{-140}$
$\beta_{K_{s,s},0}$ [cm <sup>2K<sub>s</sub>-3</sup> W <sup>-K<sub>s</sub>+1</sup> ]	$1.8 \times 10^{-94}$	$5.1 \times 10^{-138}$	$4.1 \times 10^{-138}$
$\tau_{c,s,0}$ [fs]	350	350	190
$\sigma_{s,0}$ [cm <sup>2</sup> ]	$5.47 \times 10^{-20}$	$5.47 \times 10^{-20}$	$1.01 \times 10^{-19}$